

# Analytic energy gradients for variational two-electron reduced-density matrix methods within the density-fitting approximation

J. Wayne Mullinax,<sup>1</sup> Evgeny Epifanovsky,<sup>2</sup> Gergely Gidofalvi,<sup>3</sup> and A. Eugene DePrince III<sup>1</sup>

<sup>1</sup> *Department of Chemistry and Biochemistry, Florida State University, Tallahassee, FL 32306*

<sup>2</sup> *Q-Chem, Inc., 6601 Owens Drive, Suite 105, Pleasanton, CA 94588*

<sup>3</sup> *Department of Chemistry and Biochemistry, Gonzaga University, Spokane, Washington 99258*

Analytic energy gradients are presented for a variational two-electron reduced-density-matrix-driven complete active space self-consistent field (v2RDM-CASSCF) procedure that employs the density-fitting (DF) approximation to the two-electron repulsion integrals. The DF approximation significantly reduces the computational cost of v2RDM-CASSCF gradient evaluation, in terms of both the number of floating-point operations and memory requirements, enabling geometry optimizations on much larger chemical systems than could previously be considered at this level of theory [E. Maradzike *et al.*, *J. Chem. Theory Comput.*, 2017, **13**, 4113–4122]. The efficacy of v2RDM-CASSCF for computing equilibrium geometries and harmonic vibrational frequencies is assessed using a set of 25 small closed- and open-shell molecules. Equilibrium bond lengths from v2RDM-CASSCF differ from those obtained from configuration-interaction-driven CASSCF (CI-CASSCF) by 0.62 pm and 0.05 pm, depending on whether the optimal reduced-density matrices from v2RDM-CASSCF satisfy two-particle  $N$ -representability conditions (PQG) or PQG plus partial three-particle conditions (PQG+T2), respectively. Harmonic vibrational frequencies, which are obtained by finite differences of v2RDM-CASSCF analytic energy gradients, similarly demonstrate that quantitative agreement between v2RDM- and CI-CASSCF requires the consideration of partial three-particle  $N$ -representability conditions. Lastly, optimized geometries are obtained for the lowest-energy singlet and triplet states of the linear polyacene series up to dodecacene ( $C_{50}H_{28}$ ), in which case the active space is comprised of 50 electrons in 50 orbitals. The v2RDM-CASSCF singlet-triplet energy gap extrapolated to an infinitely-long linear acene molecule is found to be 7.8 kcal mol<sup>-1</sup>.

## I. INTRODUCTION

Nondynamical correlation effects in large molecular systems are notoriously difficult to model, particularly as the number of strongly-correlated electrons increases. For small systems, the complete active space self-consistent field (CASSCF) method[1–4] provides a reliable zeroth-order description of the electronic structure that can be improved by the additional consideration of dynamical correlation effects, for example, through perturbation theory [5]. However, the steep computational scaling of configuration-interaction (CI) based descriptions of the electronic structure of the active space limits the applicability of CI-CASSCF to active spaces comprised of at most 20 electrons in 20 orbitals.[6] As a result, several approximations to CASSCF that are also based on a CI-type *ansatz* have been proposed, including the restricted active space self-consistent field,[7, 8] the generalized active space (GAS) self-consistent field,[9, 10] the split GAS,[11] the occupation-restricted multiple active spaces self-consistent field,[12] and full CI quantum Monte Carlo self-consistent field methods.[13, 14] While these methods are applicable to larger active spaces than are permitted by current CI-CASSCF implementations, abandoning the CI-based *ansatz* altogether allows one to achieve formally polynomially-scaling approximations to CASSCF. For example, one of the most popular alternatives to the CI parameterization of the wave function expansion is the density-matrix renormalization group (DMRG) approach, wherein the wave function is ex-

pressed as a matrix product state.[15–27] An approximation to CASSCF can be achieved by coupling a DMRG calculation within an active space to an orbital optimization scheme.[28–33] The result is a polynomially-scaling method that can treat large active spaces required, for example, in extended  $\pi$ -conjugated molecules, transition metal dimers, and organometallic complexes.[24]

Alternatively, the electronic structure of the active space can be described without considering *any* wave function parameterization. The key to this strategy is the realization that the electronic Hamiltonian contains at most two-body interactions, and, as such, the electronic energy can be evaluated exactly with knowledge of the two-electron reduced-density matrix (2RDM). The allure of replacing the wave function with the 2RDM lies in the fact that the latter offers a far more compact representation of electronic structure than that offered by the exact wave function. The 2RDM can be determined directly by minimizing the energy with respect to variations in its elements, subject to a set of  $N$ -representability conditions, which are constraints placed on the 2RDM to ensure that it is derived from an  $N$ -electron wave function.[34–49] By coupling an orbital optimization to a variational 2RDM (v2RDM) based description of the active space, one can achieve a v2RDM-driven approximation to CASSCF that scales polynomially with respect to the number of active orbitals.[50, 51]

We have recently described software to compute v2RDM-CASSCF energies[51] and analytic energy gradients,[52] which is available as a plugin[53] to the Psi4

electronic structure package.[54, 55] This implementation has been applied to energy computations involving active spaces as large as 50 electrons in 50 orbitals with the simultaneous optimization of 1892 orbitals.[51] The consideration of large numbers of external orbitals in energy computations is facilitated by the use of the density-fitting (DF) approximation to the electron repulsion integrals (ERIs).[56–59] which leads to significant decreases in the storage requirements and floating-point cost of the orbital optimization procedure. However, the analytic energy gradient implementation described in Ref. 52 employs only conventional ERIs, which limits its applicability to modestly sized systems and basis sets. In this paper, we describe a new implementation of analytic energy gradients for v2RDM-CASSCF that employs the DF approximation to the ERIs and is thus applicable to much larger molecular systems. This new implementation is available in version 5.1 of the Q-Chem electronic structure package.[60]

This paper is organized as follows. In Sec. II, we review the theoretical details of v2RDM-CASSCF, summarize the semidefinite optimization algorithm used within our software, and present the analytic gradient expressions. In Sec. IV, we benchmark the method by comparing v2RDM-CASSCF equilibrium geometries and harmonic vibrational frequencies for a set of 25 molecules to those computed with conventional CASSCF and to those derived from experiment. We then demonstrate the applicability of the code to large systems by computing the singlet-triplet energy gap of the linear acene series up to dodecacene ( $C_{50}H_{28}$ ) using v2RDM-CASSCF optimized geometries. Computational details can be found in Sec. III.

## II. THEORY

In this Section, we summarize the theoretical details underlying the v2RDM-CASSCF energy optimization procedure and v2RDM-CASSCF analytic gradient evaluation in the case that the ERIs are represented within the DF approximation. We employ a set of orthonormal molecular orbitals (MOs) indexed by  $p, q, r$ , and  $s$  throughout. The MOs are partitioned into a set of inactive (doubly occupied) orbitals indexed by  $i, j, k$ , and  $l$ ; a set of active orbitals indexed by  $t, u, v, w, x$ , and  $y$ ; and a set of external orbitals. When spin labels are employed and these labels are not explicitly specified as  $\alpha$  or  $\beta$ , general spin labels are indicated by  $\sigma, \tau, \kappa, \lambda, \mu$ , and  $\nu$ . The auxiliary basis functions employed within the DF approximation are indexed by  $P, Q, R$ , and  $S$ . For the sake of brevity, we will refer to v2RDM-CASSCF computations performed subject to PQG or PQG+T2 conditions simply as PQG and PQG+T2. Table I summarizes this notation.

TABLE I: Summary of Notation

Label	Summary
$p, q, r, s$	general molecular orbitals
$i, j, k, l$	inactive (doubly occupied) orbitals
$t, u, v, w, x, y$	active orbitals
$P, Q, R, S$	auxiliary basis functions
$\sigma, \tau, \kappa, \lambda, \mu, \nu$	spin functions
PQG	v2RDM-CASSCF subject to the PQG conditions
PQG+T2	v2RDM-CASSCF subject to the PQG+T2 conditions

### A. CASSCF energy and density

The non-relativistic electronic energy for a many-electron system is given by

$$E = \sum_{pq} (T_{pq} + V_{pq}) \gamma_{pq} + \sum_{pqrs} (pq|rs) \Gamma_{pqrs}, \quad (1)$$

where  $T_{pq}$  and  $V_{pq}$  represent the electron kinetic energy and electron-nuclear potential energy integrals, respectively,  $(pq|rs)$  represents an element of the ERI tensor, and  $\gamma_{pq}$  and  $\Gamma_{pqrs}$  represent elements of the spin-free one-electron reduced-density matrix (1RDM) and the spin-free 2RDM, respectively. For a CASSCF wave function,  $\gamma$  and  $\Gamma$  exhibit block structure based on the partitioning of the orbitals. The non-zero blocks of  $\gamma$  are

$$\gamma_{ij} = 2\delta_{ij}, \quad (2)$$

and

$$\gamma_{tu} = {}^1D_{u\alpha}^{t\alpha} + {}^1D_{u\beta}^{t\beta}, \quad (3)$$

and the elements of the spin blocks that comprise the active-active block of  $\gamma$  are defined as

$${}^1D_{u\sigma}^{t\sigma} = \langle \Psi | \hat{a}_{t\sigma}^\dagger \hat{a}_{u\sigma} | \Psi \rangle, \quad (4)$$

where  $\hat{a}^\dagger$  and  $\hat{a}$  represent creation and annihilation operators of second quantization, respectively. The non-zero elements of  $\Gamma$  are

$$\Gamma_{ijkl} = 2\delta_{ij}\delta_{kl} - \delta_{il}\delta_{jk}, \quad (5)$$

$$\Gamma_{ijtu} = \Gamma_{tuij} = \gamma_{tu}\delta_{ij}, \quad (6)$$

$$\Gamma_{iutj} = \Gamma_{tjiu} = -\frac{1}{2}\gamma_{tu}\delta_{ij}, \quad (7)$$

and

$$\begin{aligned} \Gamma_{tuvw} = \frac{1}{2} \bigg( & {}^2D_{u\alpha w\alpha}^{t\alpha v\alpha} + {}^2D_{u\alpha w\beta}^{t\alpha v\beta} \\ & + {}^2D_{u\beta w\alpha}^{t\beta v\alpha} + {}^2D_{u\beta w\beta}^{t\beta v\beta} \bigg), \end{aligned} \quad (8)$$

where the elements of the active-space spin-blocks are defined by

$${}^2D_{u\sigma w\tau}^{t\sigma v\tau} = \langle \Psi | \hat{a}_{t\sigma}^\dagger \hat{a}_{v\tau}^\dagger \hat{a}_{w\tau} \hat{a}_{u\sigma} | \Psi \rangle. \quad (9)$$

Given the block structure of  $\gamma$  and  $\Gamma$ , Eq. 1 can be reexpressed as

$$E = E_{\text{core}} + E_{\text{active}} \quad (10)$$

where

$$E_{\text{core}} = 2 \sum_i (T_{ii} + V_{ii}) + \sum_{ij} [2(ii|jj) - (ij|ij)], \quad (11)$$

and

$$E_{\text{active}} = \sum_{tu} h_{tu} \gamma_{tu} + \sum_{tuvw} (tu|vw) \Gamma_{tuvw}. \quad (12)$$

Here, the one-electron matrix elements,  $h_{tu}$ , are defined by

$$h_{tu} = T_{tu} + V_{tu} + \sum_i [2(ii|tu) - (iu|it)]. \quad (13)$$

The ERIs entering Eqs. 11-13 are computed using the DF approximation; we have

$$(pq|rs) \approx (pq|rs)_{\text{DF}} = \sum_P B_{pq}^P B_{rs}^P, \quad (14)$$

and the coefficients,  $B_{pq}^P$ , are determined using the Coulomb metric as

$$B_{pq}^P = \sum_Q (pq|Q) V_{QP}^{-1/2} \quad (15)$$

where

$$V_{PQ} = (P|Q) = \int d\mathbf{r}_1 \int d\mathbf{r}_2 \chi_P(\mathbf{r}_1) \chi_Q(\mathbf{r}_2) / r_{12}, \quad (16)$$

and  $\chi_P$  and  $\chi_Q$  represent auxiliary basis functions.

## B. $N$ -representability

In v2RDM-CASSCF, the active-space 2RDM is determined by minimizing the energy with respect to variations in its elements, subject to constraints intended to guarantee that the 2RDM is derivable from an ensemble of antisymmetrized  $N$ -electron wavefunctions (such a 2RDM is said to be ensemble  $N$ -representable [61]). Here, we outline some necessary ensemble  $N$ -representability conditions. First, an ensemble  $N$ -representable 2RDM is Hermitian

$${}^2D_{v_\sigma w_\tau}^{t_\sigma u_\tau} = {}^2D_{t_\sigma u_\tau}^{v_\sigma w_\tau}, \quad (17)$$

and it is antisymmetric with respect to the exchange of its indices

$${}^2D_{v_\sigma w_\tau}^{t_\sigma u_\tau} = -{}^2D_{v_\sigma w_\tau}^{u_\tau t_\sigma} = -{}^2D_{w_\tau v_\sigma}^{t_\sigma u_\tau} = {}^2D_{w_\tau v_\sigma}^{u_\tau t_\sigma}. \quad (18)$$

Second, the 2RDM should map onto the 1RDM through a set of contractions given by

$$(N_\sigma - 1) {}^1D_{u_\sigma}^{t_\sigma} = \sum_v {}^2D_{u_\sigma v_\sigma}^{t_\sigma v_\sigma}, \quad (19)$$

and

$$N_\sigma {}^1D_{u_\tau}^{t_\tau} = \sum_v {}^2D_{u_\tau v_\sigma}^{t_\tau v_\sigma} \quad \text{for } \sigma \neq \tau \quad (20)$$

where  $N_\sigma$  is the number of active electrons with spin  $\sigma$ . The trace of the 2RDM must also preserve the number of pairs of electrons, according to

$$\sum_{tu} {}^2D_{t_\sigma u_\sigma}^{t_\sigma u_\sigma} = N_\sigma (N_\sigma - 1), \quad (21)$$

and

$$\sum_{tu} {}^2D_{t_\sigma u_\tau}^{t_\sigma u_\tau} = N_\sigma N_\tau \quad \text{for } \sigma \neq \tau. \quad (22)$$

Moreover, because the eigenvalues of the 1RDM and 2RDM can be interpreted as occupation numbers for natural orbitals and geminals, respectively, both of these matrices should be positive semidefinite:

$${}^1\mathbf{D} \succeq 0 \quad (23)$$

$${}^2\mathbf{D} \succeq 0 \quad (24)$$

Additional ensemble  $N$ -representability conditions can be obtained by considering the positivity of other reduced-density matrices (RDMs) that are related to the 1RDM and 2RDM. For example, the algebra of the creation and annihilation operators implies linear relations that map the 1RDM and 2RDM to the one-hole RDM ( ${}^1\mathbf{Q}$ ), the two-hole RDM ( ${}^2\mathbf{Q}$ ), and the electron-hole RDM ( ${}^2\mathbf{G}$ ), the elements of which are defined as

$${}^1Q_{u_\sigma}^{t_\sigma} = \langle \Psi | \hat{a}_{t_\sigma} \hat{a}_{u_\sigma}^\dagger | \Psi \rangle, \quad (25)$$

$${}^2Q_{v_\sigma w_\tau}^{t_\sigma u_\tau} = \langle \Psi | \hat{a}_{t_\sigma} \hat{a}_{u_\tau} \hat{a}_{w_\tau}^\dagger \hat{a}_{v_\sigma}^\dagger | \Psi \rangle, \quad (26)$$

and

$${}^2G_{v_\kappa w_\lambda}^{t_\sigma u_\tau} = \langle \Psi | \hat{a}_{t_\sigma}^\dagger \hat{a}_{u_\tau} \hat{a}_{w_\lambda}^\dagger \hat{a}_{v_\kappa} | \Psi \rangle. \quad (27)$$

The  $N$ -representability of the 2RDM requires that each of these matrices be positive semidefinite; these constraints comprise the ‘‘PQG’’ constraints of Garrod and Percus.[34]. In this work, we also consider the partial three-body constraint that enforces the nonnegativity of the three-body RDM,  $\mathbf{T2}$ , [44, 62] with elements

$$\begin{aligned} T2_{w_\lambda x_\mu y_\nu}^{t_\sigma u_\tau v_\kappa} &= \langle \Psi | \hat{a}_{t_\sigma}^\dagger \hat{a}_{u_\tau} \hat{a}_{v_\kappa}^\dagger \hat{a}_{y_\nu} \hat{a}_{x_\mu} \hat{a}_{w_\lambda} | \Psi \rangle \\ &+ \langle \Psi | \hat{a}_{y_\nu}^\dagger \hat{a}_{x_\mu} \hat{a}_{w_\lambda} \hat{a}_{t_\sigma}^\dagger \hat{a}_{u_\tau} \hat{a}_{v_\kappa} | \Psi \rangle. \end{aligned} \quad (28)$$

For a non-relativistic Hamiltonian, we may exploit the spin-block structure of each of these RDMs; this structure is described in Refs. 48 and 51.

For a non-relativistic Hamiltonian, the 2RDM can also be constrained to satisfy ensemble spin-state conditions. For example, when Eqs. 19-21 are satisfied, we have

$\langle \hat{S}_z \rangle = \frac{1}{2}(N_\alpha - N_\beta)$ . By considering the expectation value of  $\hat{S}^2$ , we arrive at the equality

$$\sum_{tu} {}^2D_{t_\alpha u_\beta}^{t_\alpha u_\beta} = \frac{1}{2}(N_\alpha + N_\beta) + \frac{1}{4}(N_\alpha - N_\beta)^2 - S(S+1), \quad (29)$$

where  $S$  represents the total spin angular momentum quantum number. Slightly stronger [63] spin constraints can be derived for the case that the state in question is the maximal spin projection,  $|\Psi\rangle = |\Psi_{S, M_S=S}\rangle$ , by considering action of the raising operator,  $\hat{S}^+$ , on the wavefunction

$$\hat{S}^+ |\Psi_{S, M_S=S}\rangle = 0. \quad (30)$$

Equation 30 implies two sets of constraints given by

$$\langle \Psi_{S, M_S=S} | \hat{a}_t^\dagger \hat{a}_u \hat{S}^+ | \Psi_{S, M_S=S} \rangle = 0 \quad \forall t, u, \quad (31)$$

and

$$\langle \Psi_{S, M_S=S} | \hat{S}^+ \hat{a}_t^\dagger \hat{a}_u | \Psi_{S, M_S=S} \rangle = 0 \quad \forall t, u \quad (32)$$

which are expressible in terms of the elements of the particle-hole RDM as

$$\sum_v {}^2G_{t_\beta v_\alpha}^{v_\beta v_\alpha} = 0 \quad \forall t, u \quad (33)$$

$$\sum_v {}^2G_{v_\beta v_\alpha}^{t_\beta t_\alpha} = 0 \quad \forall t, u \quad (34)$$

Optimizations performed under these maximal spin constraints yield essentially the same results as those performed by enforcing the Eq. 29 alone (for the maximal spin state). We include them nonetheless because we have found that their presence sometimes improves the convergence properties of the v2RDM-CASSCF optimizations on open-shell systems.

### C. Semidefinite optimization

The minimization of Eq. 12 with respect to the elements of the active-space 2RDM, subject to the constraints outlined above, is a semidefinite optimization problem. The primal formulation of this problem is

$$\begin{aligned} &\text{minimize} \quad E_{\text{primal}} = \mathbf{c}^T \cdot \mathbf{x}, \\ &\text{such that} \quad \mathbf{A}\mathbf{x} = \mathbf{b}, \\ &\text{and} \quad M(\mathbf{x}) \succeq 0 \end{aligned} \quad (35)$$

where the vector  $\mathbf{x}$  is the primal solution vector and the vector  $\mathbf{c}$  contains the one- and two-electron integrals. The constraint matrix  $\mathbf{A}$  and constraint vector  $\mathbf{b}$  encode the  $N$ -representability conditions that  $\mathbf{x}$  must satisfy. The mapping  $M(\mathbf{x})$  maps the primal solution onto

the set of positive semidefinite active-space RDMs

$$M(\mathbf{x}) = \begin{pmatrix} {}^1\mathbf{D} & 0 & 0 & 0 & 0 & 0 \\ 0 & {}^1\mathbf{Q} & 0 & 0 & 0 & 0 \\ 0 & 0 & {}^2\mathbf{D} & 0 & 0 & 0 \\ 0 & 0 & 0 & {}^2\mathbf{Q} & 0 & 0 \\ 0 & 0 & 0 & 0 & {}^2\mathbf{G} & 0 \\ 0 & 0 & 0 & 0 & 0 & \mathbf{T2} \end{pmatrix}. \quad (36)$$

The corresponding dual formulation of the problem is

$$\begin{aligned} &\text{maximize} \quad E_{\text{dual}} = \mathbf{b}^T \cdot \mathbf{y}, \\ &\text{such that} \quad \mathbf{z} = \mathbf{c} - \mathbf{A}^T \mathbf{y}, \\ &\text{and} \quad M(\mathbf{z}) \succeq 0, \end{aligned} \quad (37)$$

where the vectors  $\mathbf{y}$  and  $\mathbf{z}$  are the dual solution vectors.

The optimal RDMs are determined using a boundary-point semidefinite optimization algorithm.[64–66] This approach maximizes the augmented Lagrangian for the dual problem

$$\mathcal{L}_{\text{act}} = \mathbf{b}^T \mathbf{y} - \mathbf{x}^T (\mathbf{A}^T \mathbf{y} - \mathbf{c} + \mathbf{z}) - \frac{1}{2\mu} \|\mathbf{A}^T \mathbf{y} - \mathbf{c} + \mathbf{z}\|^2 \quad (38)$$

by the following two-step procedure:

1. Solve  $\mathbf{A}\mathbf{A}^T \mathbf{y} = \mathbf{A}(\mathbf{c} - \mathbf{z}) + \mu(\mathbf{b} - \mathbf{A}\mathbf{x})$  for  $\mathbf{y}$  by conjugate gradient methods.
2. Update  $\mathbf{x}$  and  $\mathbf{z}$  by separating  $\mathbf{U} = M(\mu\mathbf{x} + \mathbf{A}^T \mathbf{y} - \mathbf{c})$  into its positive and negative components (by diagonalization). The updated primal and dual solutions  $\mathbf{x}$  and  $\mathbf{z}$  are given by  $M(\mathbf{x}) = \mathbf{U}(+)/\mu$  and  $M(\mathbf{z}) = -\mathbf{U}(-)$ .

The penalty parameter  $\mu$  is dynamically updated during the course of the v2RDM calculation.[66] The v2RDM optimization is considered converged when

$$\|\mathbf{A}\mathbf{x} - \mathbf{b}\| < \epsilon_{\text{error}}, \quad (39)$$

$$\|\mathbf{A}^T \mathbf{y} - \mathbf{c} + \mathbf{z}\| < \epsilon_{\text{error}}, \quad (40)$$

and

$$|E_{\text{primal}} - E_{\text{dual}}| < \epsilon_{\text{gap}}, \quad (41)$$

for given thresholds  $\epsilon_{\text{error}}$  and  $\epsilon_{\text{gap}}$ .

### D. Orbital optimization

In v2RDM-CASSCF, the energy is minimized with respect to both the elements of the RDMs and the orbital parameters. We employ an algorithm in which the orbitals are optimized after a preselected number of v2RDM iterations (steps 1 and 2 in Sec. II C) or after the v2RDM optimization converges. Because the v2RDM-CASSCF energy is invariant to rotations among inactive, active, or external orbitals, the energy is optimized with

respect to rotations between inactive and active, inactive and virtual, and active and virtual orbitals. The optimization utilizes an exponential parameterization of the orbital transformation matrix  $\mathbf{U} = e^{\mathbf{K}}$ , where the skew-symmetric matrix  $\mathbf{K}$  contains the nonredundant rotation parameters. The unique matrix elements of  $\mathbf{K}$  can be organized into the vector  $\boldsymbol{\kappa}$ , and the energy expression, truncated at second order in  $\boldsymbol{\kappa}$ , is

$$E(\boldsymbol{\kappa}) = E(\mathbf{0}) + \boldsymbol{\kappa}^T \mathbf{g} + \frac{1}{2} \boldsymbol{\kappa}^T \mathbf{B} \boldsymbol{\kappa}. \quad (42)$$

The energy is minimized with respect to the orbital parameters using a quasi-Newton approach that only requires the computation of the orbital gradient ( $\mathbf{g}$ ) and diagonal elements of the orbital Hessian ( $\mathbf{B}$ ). For details of the orbital optimization procedure, the reader is referred to Ref. 51. We consider the orbitals to be converged when the norm of the orbital gradient falls below the threshold  $\epsilon_{\text{ograd}}$  and the energy computed before and after the orbitals optimization step differs by less than  $\epsilon_{\text{oene}}$ .

### E. Analytic gradients

To facilitate the derivation of the analytic gradients, we define the Lagrangian

$$\mathcal{L} = E_{\text{core}} + \mathcal{L}_{\text{act}}, \quad (43)$$

which is stationary with respect to variations in the active-space 1-RDM and 2-RDM (the reader is referred to Ref. 52 for a discussion on the stationarity of  $\mathcal{L}_{\text{act}}$ ). The gradient of the energy with respect to an arbitrary perturbation  $\chi$  is

$$\begin{aligned} \frac{dE}{d\chi} = \frac{\partial \mathcal{L}}{\partial \chi} = & \sum_{pq} (T_{pq}^{\chi} + V_{pq}^{\chi}) \gamma_{pq} \\ & + \sum_{pqrs} (pq|rs)_{\text{DF}}^{\chi} \Gamma_{pqrs} - \sum_{pq} X_{pq} S_{pq}^{\chi} \end{aligned} \quad (44)$$

where  $T_{pq}^{\chi}$ ,  $V_{pq}^{\chi}$ , and  $S_{pq}^{\chi}$  are the kinetic energy, electron-nucleus potential energy, and overlap derivative integrals, respectively. The term involving the electron repulsion derivative integrals,  $(pq|rs)_{\text{DF}}^{\chi}$ , is evaluated as[67]

$$\begin{aligned} \sum_{pqrs} (pq|rs)_{\text{DF}}^{\chi} \Gamma_{pqrs} = & 2 \sum_{pq} \sum_P \Gamma_{pq}^P (P|pq)^{\chi} \\ & - \sum_{PQ} \Gamma_{PQ} V_{PQ}^{\chi} \end{aligned} \quad (45)$$

where

$$\Gamma_{pq}^P = \sum_{rs} \sum_Q \Gamma_{pqrs} B_{rs}^Q V_{QP}^{-1/2}, \quad (46)$$

and

$$\Gamma_{PQ} = \sum_{pq} \sum_R \Gamma_{pq}^P \Gamma_{pq}^R V_{RQ}^{-1/2}. \quad (47)$$

Although we present the gradient expressions in the MO basis, in practice, the gradient is evaluated in the AO basis. As such, the 1RDM and 2RDM must be transformed to the AO basis before contraction with the derivative integrals. Within the DF approximation, only two- and three-index quantities enter Eq. 44, meaning that we avoid the cost associated with transforming the full 2RDM to the AO basis, as was done in our previous implementation. This restructuring of the algorithm results in tremendous computational savings for derivative computations on large systems.

The last term in Eq. 44 arises from the orbital response to the perturbation. It can be shown[68] that for a CASSCF wave function with an energy that is stationary with respect to rotations between all nonredundant orbital pairs, the orbital response depends only on the overlap derivative integrals and the orbital Lagrangian,  $\mathbf{X}$ , with matrix elements

$$X_{pq} = \sum_r (T_{pr} + V_{pr}) \gamma_{rq} + 2 \sum_{rst} (pr|st) \Gamma_{qrst} \quad (48)$$

### III. COMPUTATIONAL DETAILS

All v2RDM-CASSCF and B3LYP calculations were carried out in development version of Q-Chem 5.1. For geometry optimizations, v2RDM-CASSCF calculations were considered converged when  $\epsilon_{\text{error}} < 1.0 \times 10^{-6}$ ,  $\epsilon_{\text{gap}} < 1.0 \times 10^{-4} E_h$ ,  $\epsilon_{\text{ograd}} < 1.0 \times 10^{-6} E_h$ , and  $\epsilon_{\text{oene}} < 1.0 \times 10^{-10} E_h$ . Geometry optimizations were considered converged when the maximum gradient component reached  $1.5 \times 10^{-5} E_h a_0^{-1}$  and either the maximum atomic displacement was less than  $6.0 \times 10^{-5} a_0$  or the energy change of successive optimization cycles was less than  $1.0 \times 10^{-8} E_h$ . Harmonic vibrational frequencies were computed by finite differences of the analytic energy gradients using a 5-point stencil with a displacement of 0.005 Å, and the “sow/reap” mode in the Psi4 software package was used to generate symmetry-adapted displacements. For the frequency calculations, we tightened the convergence criteria to  $\epsilon_{\text{error}} < 1.0 \times 10^{-8}$ ,  $\epsilon_{\text{gap}} < 1.0 \times 10^{-8} E_h$ ,  $\epsilon_{\text{ograd}} < 1.0 \times 10^{-8} E_h$ , and  $\epsilon_{\text{oene}} < 1.0 \times 10^{-11} E_h$ . However, we note that we encountered some difficulties in converging some PQG+T2 computations this tightly. In these cases (which are noted in Table V), the convergence criteria were loosened to  $\epsilon_{\text{error}} < 1.0 \times 10^{-6}$ ,  $\epsilon_{\text{gap}} < 1.0 \times 10^{-6} E_h$ ,  $\epsilon_{\text{ograd}} < 1.0 \times 10^{-6} E_h$ , and  $\epsilon_{\text{oene}} < 1.0 \times 10^{-9} E_h$ . We used finite difference frequency calculations to estimate the error introduced by the loose convergence thresholds. Computations were performed at the PQG level of theory using both sets of thresholds, and we estimate this error to be less than  $\text{cm}^{-1}$ , except in the case of the low-frequency mode for HNC which exhibited larger errors (see Supporting Information).

All CI-CASSCF calculations were performed using the GAMESS software package.[69] The CI-CASSCF cal-

TABLE II: Term symbols and active spaces for the small molecules that comprise our test set.

Molecule	Term	Active Space
BF	$^1\Sigma^+$	(10,8)
BH	$^1\Sigma^+$	(4,5)
C <sub>2</sub>	$^1\Sigma_g^+$	(8,8)
CH <sub>2</sub>	$^1A_1$	(6,6)
CH <sub>4</sub>	$^1A_1$	(8,8)
CO	$^1\Sigma^+$	(10,8)
F <sub>2</sub>	$^1\Sigma_g^+$	(14,8)
H <sub>2</sub> O	$^1A_1$	(8,6)
HCN	$^1\Sigma^+$	(10,9)
HF	$^1\Sigma^+$	(8,5)
HNC	$^1\Sigma^+$	(10,9)
HNO	$^1A'$	(12,9)
HOF	$^1A'$	(14,9)
N <sub>2</sub>	$^1\Sigma_g^+$	(10,8)
N <sub>2</sub> H <sub>2</sub>	$^1A_g$	(12,10)
NH <sub>3</sub>	$^1A_1$	(8,7)
BO	$^2\Sigma^+$	(9,8)
CH	$^2\Pi$	(5,5)
NH <sub>2</sub>	$^2B_1$	(7,6)
OH	$^2\Pi$	(7,5)
B <sub>2</sub>	$^3\Sigma_g^-$	(6,8)
CH <sub>2</sub>	$^3B_1$	(6,6)
NF	$^3\Sigma^-$	(12,8)
NH	$^3\Sigma^-$	(6,5)
O <sub>2</sub>	$^3\Sigma_g^-$	(12,8)

culations were considered converged when the maximum asymmetry in the Lagrangian matrix fell below  $1.0 \times 10^{-7} E_h$  and the energy change was smaller than  $1.0 \times 10^{-10} E_h$ . The CI-CASSCF geometry optimizations were considered converged when the largest component of the gradient was below  $1.0 \times 10^{-7} E_h a_0^{-1}$  and the root mean square gradient was less than  $\frac{1}{3} \times 10^{-7} E_h a_0^{-1}$ . Harmonic vibrational frequencies were computed with GAMESS using analytic Hessians, which are available for basis sets comprised of *s*, *p*, and *d* functions. Therefore, we report harmonic frequencies for the cc-pVDZ basis set only.

All calculations employed the cc-pVXZ[70] (*X* = D, T, Q) basis sets. The cc-pVXZ-JK[71] auxiliary basis sets were used in the DF approximation for the v2RDM-CASSCF computations. The cc-pVDZ-JK basis set is formed by removing the highest angular momentum functions from the cc-pVTZ-JK basis set.

## IV. RESULTS AND DISCUSSION

### A. Benchmark computations: equilibrium geometries

We optimized the geometries for the 25 molecules listed in Table II using CI- and v2RDM-CASSCF with a full-valence active space. Table III presents the error in the CI- and v2RDM-CASSCF bond lengths relative to those derived from experiment. Agreement with experimental geometries generally improves with the size of the

basis set for both CI- and v2RDM-CASSCF. For the cc-pVQZ basis set, the mean unsigned error for the bond lengths are 1.0 pm, 1.6 pm, and 1.1 pm for CI-CASSCF, PQG, and PQG+T2, respectively. The unsigned errors are under 2.0 pm for CI-CASSCF and PQG+T2 using the cc-pVQZ basis except for two cases (F<sub>2</sub> and B<sub>2</sub>). In general, bond lengths obtained from PQG tend to deviate more from experiment than those from PQG+T2 or CI-CASSCF.

Table IV provides errors in the CI- and v2RDM-CASSCF bond angles relative to those derived from experiment. Again, in general, these errors decrease with the size of the basis set. For the cc-pVQZ basis set the errors are all below 5.0° with mean unsigned errors of 1.5°, 1.7°, and 1.5° for CI-CASSCF, PQG, and PQG+T2, respectively. For this test set, v2RDM- and CI-CASSCF provide predictions in bond angles that are generally similar in quality, when comparing to angles derived from experiment. For example, CI-CASSCF and PQG+T2 both underestimate all bond angles with the exception of the H–N–O angle in HNO. The H–N–N angle in N<sub>2</sub>H<sub>2</sub> is also overestimated when using PQG within the cc-pVTZ and cc-pVQZ basis sets. Although the maximum error for each level of theory exceeds 4.0° (CH<sub>2</sub>), all other bond angles agree with those from experiment to within 2.0°.

Figure 1 illustrates the difference between the CI- and v2RDM-CASSCF bond lengths in the cc-pVXZ basis sets (*X* = D, T, Q). In general, these differences are insensitive to the size of the one-electron basis. The mean unsigned differences between the CI-CASSCF and PQG bond lengths are 0.67 pm, 0.74 pm, and 0.62 pm for the cc-pVDZ, cc-pVTZ, and cc-pVQZ, respectively. The mean unsigned differences in these basis sets decrease to, at most, 0.06 pm when the T2 condition is enforced. Similarly, the mean unsigned difference between the CI- and PQG bond angles is 0.4° for all basis sets and falls to 0.0° when enforcing the PQG+T2 conditions. These results demonstrate that the PQG+T2 conditions lead to quantitative agreement between CI- and v2RDM-CASSCF geometries. We recently reported similar deviations between CI- and v2RDM-CASSCF bond lengths and angles for a test set of 20 molecules with singlet spin states using analytic energy gradients and conventional (non-DF) ERIs.[52] The present results extend these observations to the case of non-singlet molecules and to gradients computed within the DF approximation. As seen in Fig. 1 (and in Ref. 52) v2RDM-CASSCF bond lengths are typically longer than those from CI-CASSCF. This effect can be rationalized in terms of the “over correlation” problem of v2RDM methods; for small molecules, more approximate *N*-representability conditions lead to longer bond lengths.

We note two clear outliers in Fig. 1, which correspond to bond lengths for C<sub>2</sub> and B<sub>2</sub> optimized under the PQG conditions. The CI-CASSCF wave functions for these two molecules exhibit the most multiconfigurational character in the entire set, as measured by the magnitude of the largest CI-coefficients in the respective expansions

TABLE III: Errors in computed equilibrium bond lengths ( $\Delta r_e$ , pm)<sup>a</sup> from CI- and v2RDM-CASSCF using the cc-pVXZ (X = D, T, Q) basis sets. Computed bond lengths are compared to those obtained from experiment ( $r_e$ , Å). All values of  $r_e$  were taken from Ref. 72 and the references therein.

Molecule	Term	Bond	$r_e$	$\Delta r_e$								
				cc-pVDZ			cc-pVTZ			cc-pVQZ		
				CI	PQG	PQG+T2	CI	PQG	PQG+T2	CI	PQG	PQG+T2
BF	<sup>1</sup> $\Sigma^+$	B-F	1.267	2.4	2.5	2.5	0.1	0.1	0.1	-0.2	-0.2	-0.2
BH	<sup>1</sup> $\Sigma^+$	H-B	1.232	3.5	4.1	3.5	1.9	2.5	1.9	1.7	2.3	1.7
C <sub>2</sub>	<sup>1</sup> $\Sigma_g^+$	C-C	1.242	2.4	7.1	2.8	1.3	5.8	1.7	1.1	5.5	1.5
CH <sub>2</sub>	<sup>1</sup> $A_1$	H-C	1.107	3.2	3.6	3.2	1.8	2.3	1.8	1.7	2.2	1.7
CH <sub>4</sub>	<sup>1</sup> $A_1$	H-C	1.087	2.5	3.2	2.5	1.4	2.2	1.5	1.4	2.2	1.4
CO	<sup>1</sup> $\Sigma^+$	C-O	1.128	1.4	1.8	1.4	0.7	1.1	0.8	0.5	0.9	0.5
F <sub>2</sub>	<sup>1</sup> $\Sigma_g^+$	F-F	1.412	10.5	10.5	10.5	4.9	4.9	4.9	4.8	4.8	4.8
H <sub>2</sub> O	<sup>1</sup> $A_1$	H-O	0.958	1.3	1.4	1.3	0.6	0.7	0.6	0.5	0.6	0.5
HCN	<sup>1</sup> $\Sigma^+$	H-C	1.064	2.4	3.0	2.4	-0.7	1.9	-0.7	-0.7	-0.6	-0.7
		C-N	1.156	1.9	2.8	2.0	0.4	1.7	0.5	0.3	0.8	0.3
HF	<sup>1</sup> $\Sigma^+$	H-F	0.917	0.5	0.5	0.5	0.0	0.0	0.0	-0.2	-0.2	-0.2
HNC	<sup>1</sup> $\Sigma^+$	H-N	0.986	2.5	3.3	2.5	1.6	2.4	1.7	1.6	2.4	1.6
		C-N	1.173	1.6	2.5	1.7	0.5	1.3	0.5	0.3	1.2	0.4
HNO	<sup>1</sup> $A'$	H-N	1.090	-0.2	0.0	-0.2	-1.3	-1.1	-1.2	-1.4	-1.3	-1.3
		N-O	1.209	0.6	1.4	0.7	0.2	1.0	0.3	0.0	0.8	0.1
HOF	<sup>1</sup> $A'$	H-O	0.960	1.9	2.2	2.0	1.2	1.4	1.2	1.0	1.3	1.1
		O-F	1.442	4.9	5.4	4.9	2.1	2.6	2.1	1.9	2.4	1.9
N <sub>2</sub>	<sup>1</sup> $\Sigma_g^+$	N-N	1.098	1.9	2.3	1.9	0.8	1.3	0.9	0.6	1.1	0.7
N <sub>2</sub> H <sub>2</sub>	<sup>1</sup> $A_g$	H-N	1.028	2.5	3.3	2.6	1.5	2.3	1.6	1.4	2.2	1.4
		N-N	1.252	1.3	1.3	1.4	0.7	0.7	0.8	0.5	0.5	0.6
NH <sub>3</sub>	<sup>1</sup> $A_1$	H-N	1.012	2.2	2.5	2.2	1.1	1.5	1.1	0.9	1.3	1.0
BO	<sup>2</sup> $\Sigma^+$	B-O	1.204	1.3	1.9	1.4	0.9	1.5	1.0	0.6	1.2	0.7
CH	<sup>2</sup> $\Pi$	H-C	1.120	2.7	2.5	2.7	1.3	1.2	1.3	1.1	1.0	1.1
NH <sub>2</sub>	<sup>2</sup> $B_1$	H-N	1.024	2.3	2.6	2.3	1.3	1.6	1.3	1.2	1.4	1.2
OH	<sup>2</sup> $\Pi$	H-O	0.970	1.3	1.3	1.3	0.5	0.5	0.5	0.3	0.3	0.3
B <sub>2</sub>	<sup>3</sup> $\Sigma_g^-$	B-B	1.590	3.9	8.2	4.3	2.7	7.0	3.1	2.4	6.7	2.9
CH <sub>2</sub>	<sup>3</sup> $B_1$	H-C	1.085	1.7	1.9	1.7	0.5	0.7	0.5	0.4	0.7	0.4
NF	<sup>3</sup> $\Sigma^-$	N-F	1.317	1.7	1.8	1.7	0.9	1.0	0.9	0.8	0.9	0.8
NH	<sup>3</sup> $\Sigma^-$	H-N	1.036	2.3	2.3	2.3	1.1	1.1	1.1	1.0	1.0	1.0
O <sub>2</sub>	<sup>3</sup> $\Sigma_g^-$	O-O	1.208	1.3	2.0	1.4	1.0	1.7	1.1	0.8	1.4	0.9
		MSE <sup>b</sup>	—	2.3	3.0	2.4	1.0	1.8	1.1	0.9	1.5	0.9
		MUE <sup>c</sup>	—	2.3	3.0	2.4	1.2	1.8	1.2	1.0	1.6	1.1
		Max <sup>d</sup>	—	10.5	10.5	10.5	4.9	7.0	4.9	4.8	6.7	4.8

<sup>a</sup>  $\Delta r_e = r_e^{\text{CASSCF}} - r_e$ . <sup>b</sup> mean signed error. <sup>c</sup> mean unsigned error. <sup>d</sup> maximum unsigned error.

TABLE IV: Errors in computed equilibrium bond angles ( $\Delta \theta_e$ , degrees)<sup>a</sup> from CI- and v2RDM-CASSCF using the cc-pVXZ (X=D,T,Q) basis sets. Computed bond angles are compared to those obtained from experiment ( $\theta_e$ , degrees). All values of  $\theta_e$  were taken from Ref. 72 and the references therein.

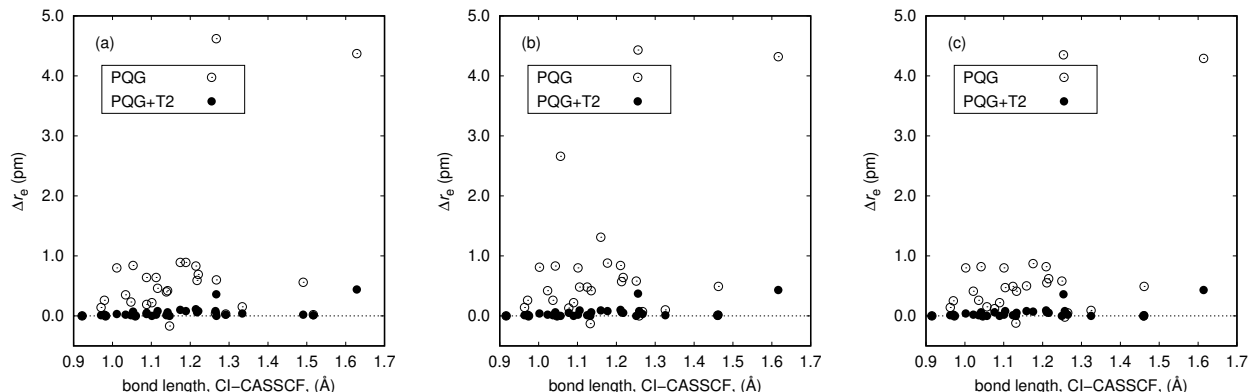
Molecule	Term	Bond	$\theta_e$	$\Delta \theta_e$								
				cc-pVDZ			cc-pVTZ			cc-pVQZ		
				CI	PQG	PQG+T2	CI	PQG	PQG+T2	CI	PQG	PQG+T2
CH <sub>2</sub>	<sup>1</sup> $A_1$	H-C-H	102.4	-2.4	-1.8	-2.4	-1.4	-1.0	-1.4	-1.2	-0.9	-1.2
H <sub>2</sub> O	<sup>1</sup> $A_1$	H-O-H	104.5	-3.3	-3.5	-3.3	-1.9	-2.1	-1.9	-1.6	-1.8	-1.6
HNO	<sup>1</sup> $A'$	H-N-O	108.0	0.5	1.1	0.5	0.9	1.4	0.9	1.0	1.5	1.0
HOF	<sup>1</sup> $A'$	H-O-F	97.2	-1.3	-1.6	-1.3	-0.2	-0.5	-0.2	-0.1	-0.4	-0.1
N <sub>2</sub> H <sub>2</sub>	<sup>1</sup> $A_g$	H-N-N	106.3	-1.3	-0.1	-1.3	-0.6	0.5	-0.7	-0.5	0.7	-0.5
NH <sub>3</sub>	<sup>1</sup> $A_1$	H-N-H	106.7	-3.9	-3.6	-3.9	-2.1	-2.1	-2.1	-1.8	-1.7	-1.8
NH <sub>2</sub>	<sup>2</sup> $B_1$	H-N-H	103.4	-3.2	-3.1	-3.2	-1.9	-2.0	-1.9	-1.6	-1.7	-1.7
CH <sub>2</sub>	<sup>3</sup> $B_1$	H-C-H	135.5	-4.5	-4.9	-4.5	-4.2	-4.5	-4.2	-4.2	-4.5	-4.2
		MSE <sup>b</sup>	—	-2.4	-2.2	-2.4	-1.4	-1.3	-1.5	-1.2	-1.1	-1.3
		MUE <sup>c</sup>	—	2.5	2.5	2.5	1.7	1.8	1.7	1.5	1.7	1.5
		Max <sup>d</sup>	—	4.5	4.9	4.5	4.2	4.5	4.2	4.2	4.5	4.2

<sup>a</sup>  $\Delta \theta_e = \theta_e^{\text{CASSCF}} - \theta_e$ . <sup>b</sup> mean signed error. <sup>c</sup> mean unsigned error. <sup>d</sup> maximum unsigned error.

(0.83 for C<sub>2</sub> and 0.88 for B<sub>2</sub>). For all other molecules considered herein, the largest CI-coefficient is greater than 0.95, with the exception of CH<sub>4</sub>, which has a leading CI-coefficient of 0.92. These outliers suggest that the PQG conditions are insufficient to correctly describe the static

correlation effects in B<sub>2</sub> and C<sub>2</sub>.

FIG. 1: Difference in equilibrium bond lengths ( $\Delta r_e$ , pm;  $\Delta r_e = r_e^{\text{v2RDM}} - r_e^{\text{CI}}$ ) obtained from full-valence v2RDM- and CI-CASSCF using the (a) cc-pVDZ, (b) cc-pVTZ, and (c) cc-pVQZ basis sets. The bond lengths considered correspond to those that are provided in Table III.



### B. Benchmark computations: harmonic vibrational frequencies

In this section, we evaluate the quality of v2RDM-CASSCF harmonic vibrational frequencies computed from finite differences of analytic energy gradients. Table V presents the error in the harmonic frequencies obtained from CI- and v2RDM-CASSCF within the cc-pVDZ basis set, as compared to those derived from experiment. The mean unsigned errors are  $64 \text{ cm}^{-1}$ ,  $84 \text{ cm}^{-1}$ , and  $65 \text{ cm}^{-1}$  at the CI-CASSCF, PQG, PQG+T2 levels of theory, respectively. The percent error is less than 9% for all CI-CASSCF frequencies, with the exception of four cases: (1) the  $\Sigma_g$  stretch of  $\text{F}_2$  (-33%), (2) the  $3A'$  bend of  $\text{HOF}$  (-16%), (3) the  $2A_1$  wagging mode of  $\text{NH}_3$  (29%), and (4) the  $2A_1$  bend of triplet  $\text{CH}_2$  (17%). The frequencies from PQG+T2 agree with those from CI-CASSCF for these four cases. For the remaining modes, the PQG+T2 frequencies similarly agree with those from experiment to within 9%. On the other hand, frequencies computed with the PQG conditions alone are less reliable; eight modes are predicted incorrectly by more than 10%, with the worst offender having a -51% error (the doubly-degenerate  $\Pi$  bend in  $\text{HNC}$ ).

Figure 2 illustrates the difference between harmonic frequencies obtained from v2RDM-CASSCF (enforcing both the PQG and PQG+T2 conditions) and CI-CASSCF. It is clear that the consideration of the T2 condition dramatically improves the agreement between v2RDM- and CI-CASSCF. We find only two modes for which the PQG constraints alone provide better agreement with CI-CASSCF: (1) the  $3A'$  bend of  $\text{HNO}$  and (2) the  $3A_g$  mode of  $\text{N}_2\text{H}_2$ . However, we note that the discrepancies between CI-CASSCF and PQG+T2 frequencies are quite small in these cases (less than  $10 \text{ cm}^{-1}$ ). For PQG, the percent difference in the predicted frequencies, relative to CI-CASSCF, is less than 4% in all but four cases: (1) the  $\Sigma_g$  stretch of  $\text{C}_2$  (-19%), (2) the  $\Pi$

bend of  $\text{HCN}$  (-16%), (3) the  $\Pi$  bend of  $\text{HNC}$  (-51%), and (4) the  $\Sigma_g$  stretch  $\text{B}_2$  (-14%). The agreement with CI-CASSCF is significantly improved upon considering the T2 condition, in which case the percent differences are less than 1% in all but two cases: (1) the  $\Sigma_g$  stretch of  $\text{C}_2$  (-1%) and (2) the  $\Sigma_g$  stretch of  $\text{B}_2$  (-2%). The mean unsigned differences between v2RDM- and CI-CASSCF frequencies are  $44 \text{ cm}^{-1}$  and  $4 \text{ cm}^{-1}$  when optimized RDMs satisfy the PQG and PQG+T2 constraints, respectively. In general, we note that the v2RDM-CASSCF frequencies are lower than those predicted by CI-CASSCF. Of the 52 frequencies considered, only five PQG and three PQG+T2 frequencies are significantly (more than  $0.5 \text{ cm}^{-1}$ ) higher than the corresponding CI-CASSCF frequency. It appears that the over-correlation associated with approximate  $N$ -representability manifests itself in generally underestimated harmonic frequencies.

### C. Linear acenes: equilibrium geometries and singlet-triplet gap

The linear polyacene series exhibits complex electronic structure, and an extensive literature considers the relative ordering of the lowest-energy singlet and triplet states, as well as the degree to which the singlet states of larger members of the series can be considered as having polyradical character. [48, 50, 51, 73–82] Here, we demonstrate the applicability of our v2RDM-CASSCF energy gradient implementation to large molecules with large active spaces by reporting equilibrium geometries and adiabatic singlet-triplet energy gaps for the linear polyacene series up to dodecacene. The active space is chosen to be comprised of the  $\pi$ -MO network, which, for an acene molecule consisting of  $k$  fused six-membered rings, corresponds to a  $(4k+2, 4k+2)$  active space. For dodecacene, the active space consists of 50 electrons in 50 orbitals.



TABLE V: Errors in computed harmonic vibrational frequencies ( $\Delta\omega_e$ ,  $\text{cm}^{-1}$ )<sup>a</sup> computed using CI- and v2RDM-CASSCF for the cc-pVDZ basis set. Computed frequencies are compared to those obtained from experiment ( $\omega_e$ ,  $\text{cm}^{-1}$ ). All values of  $\omega_e$  were taken from Ref. 72 and the references therein.

Molecule	Term	Mode	Sym	$\omega_e$	$\Delta\omega_e$		
					CI	PQG	PQG+T2
BF	$^1\Sigma^+$	1	$\Sigma$	1402	-67	-68	-68 <sup>b</sup>
BH	$^1\Sigma^+$	1	$\Sigma$	2367	-100	-139	-99
C <sub>2</sub>	$^1\Sigma_g^+$	1	$\Sigma_g$	1855	-5	-363	-31
CH <sub>2</sub>	$^1A_1$	1	A <sub>1</sub>	2806	-14	-45	-16
		2	A <sub>1</sub>	1353	64	9	64
		3	B <sub>2</sub>	2865	-11	-19	-12
CH <sub>4</sub>	$^1A_1$	1	A <sub>1</sub>	2917	22	-34	20 <sup>b</sup>
		2	E	1534	22	-9	22 <sup>b</sup>
		3	T <sub>2</sub>	3019	49	66	48 <sup>b</sup>
		4	T <sub>2</sub>	1306	34	25	33 <sup>b</sup>
CO	$^1\Sigma^+$	1	$\Sigma$	2170	-5	-43	-11
F <sub>2</sub>	$^1\Sigma_g^+$	1	$\Sigma_g$	917	-304	-305	-304
H <sub>2</sub> O	$^1A_1$	1	A <sub>1</sub>	3657	65	42	62
		2	A <sub>1</sub>	1595	121	114	121
		3	B <sub>2</sub>	3756	78	55	79
HCN	$^1\Sigma^+$	1	$\Sigma$	3312	59	7	55 <sup>b</sup>
		2	$\Sigma$	2089	6	-65	-4 <sup>b</sup>
		3	$\Pi$	712	10	-107	7 <sup>b</sup>
HF	$^1\Sigma^+$	1	$\Sigma$	4138	-83	-83	-83
HNC	$^1\Sigma^+$	1	$\Sigma$	3653	84	-14	79 <sup>b</sup>
		2	$\Sigma$	2029	14	-59	6 <sup>b</sup>
		3	$\Pi$	477	-1	-245	-5 <sup>b</sup>
HNO	$^1A'$	1	A'	2684	-48	-26	-54
		2	A'	1565	36	15	29
		3	A'	1501	39	42	33
HOF	$^1A'$	1	A'	3537	125	88	121 <sup>b</sup>
		2	A'	1393	-67	-80	-69 <sup>b</sup>
		3	A'	886	-140	-150	-140 <sup>b</sup>
N <sub>2</sub>	$^1\Sigma_g^+$	1	$\Sigma_g$	2359	-4	-54	-15
N <sub>2</sub> H <sub>2</sub>	$^1A_g$	1	A <sub>g</sub>	3058	37	-65	26 <sup>b</sup>
		2	A <sub>g</sub>	1583	37	30	35 <sup>b</sup>
		3	A <sub>g</sub>	1529	20	16	12 <sup>b</sup>
		4	A <sub>u</sub>	1289	27	-10	25 <sup>b</sup>
		5	B <sub>u</sub>	3120	3	-73	-5 <sup>b</sup>
		6	B <sub>u</sub>	1316	37	28	35 <sup>b</sup>
NH <sub>3</sub>	$^1A_1$	1	A <sub>1</sub>	3337	-9	-52	-13
		2	A <sub>1</sub>	950	279	257	280
		3	E	3444	8	-18	5
		4	E	1627	81	62	81
BO	$^2\Sigma^+$	1	$\Sigma$	1886	-14	-61	-19 <sup>b</sup>
CH	$^2\Pi$	1	$\Sigma$	2859	-114	-83	-114 <sup>b</sup>
NH <sub>2</sub>	$^2B_1$	1	A <sub>1</sub>	3219	-5	-30	-7 <sup>b</sup>
		2	A <sub>1</sub>	1497	76	68	76 <sup>b</sup>
		3	B <sub>2</sub>	3301	6	-19	5 <sup>b</sup>
OH	$^2\Pi$	1	$\Sigma$	3738	-130	-130	-130
B <sub>2</sub>	$^3\Sigma_g^-$	1	$\Sigma_g$	1051	-32	-173	-51
CH <sub>2</sub>	$^3B_1$	1	A <sub>1</sub>	2806	245	218	245 <sup>b</sup>
		2	A <sub>1</sub>	963	160	193	160 <sup>b</sup>
		3	B <sub>2</sub>	3190	71	42	70 <sup>b</sup>
NF	$^3\Sigma^-$	1	$\Sigma$	1141	-65	-67	-66 <sup>b</sup>
NH	$^3\Sigma^-$	1	$\Sigma$	3282	-171	-171	-171
O <sub>2</sub>	$^3\Sigma_g^-$	1	$\Sigma_g$	1580	-51	-108	-62 <sup>b</sup>
				MSE <sup>c</sup>	-	9	6
				MUE <sup>d</sup>	-	64	65
				Max <sup>e</sup>	-	304	304

<sup>a</sup>  $\Delta\omega_e = \omega_e^{\text{CASSCF}} - \omega_e$ . <sup>b</sup> "loose" convergence criteria used (Sec. III). <sup>c</sup> mean signed error. <sup>d</sup> mean unsigned error. <sup>e</sup> maximum unsigned error.

Figure 3 shows the adiabatic singlet-triplet excitation energies computed at the PQG/cc-pVDZ, DMRG-driven complete active space CI (CASSCF)/DZ,[75] and quantum Monte Carlo (QMC) [82] levels of theory, along with vertical excitation energies derived from the particle-particle random phase approximation (PP-RPA, using the cc-

pVDZ basis)[81] and experiment.[83–86] The QMC results taken from Ref. 82 were obtained using a Jastrow single determinant (JSD) wave function, optimized using lattice regularized diffusion Monte Carlo (LRDMC). PP-RPA, DMRG-CASSCF, PQG, and experiment are all in reasonable agreement for the smaller members of

FIG. 2: Difference in equilibrium harmonic vibrational frequencies ( $\Delta\omega_e = \omega_e^{\text{v2RDM}} - \omega_e^{\text{CI}}$ ) obtained from full-valence v2RDM- and CI-CASSCF using the cc-pVDZ basis sets. The cc-pVDZ-JK auxiliary basis set was used in the v2RDM-CASSCF optimizations. The frequencies considered correspond to those that are provided in Table V.

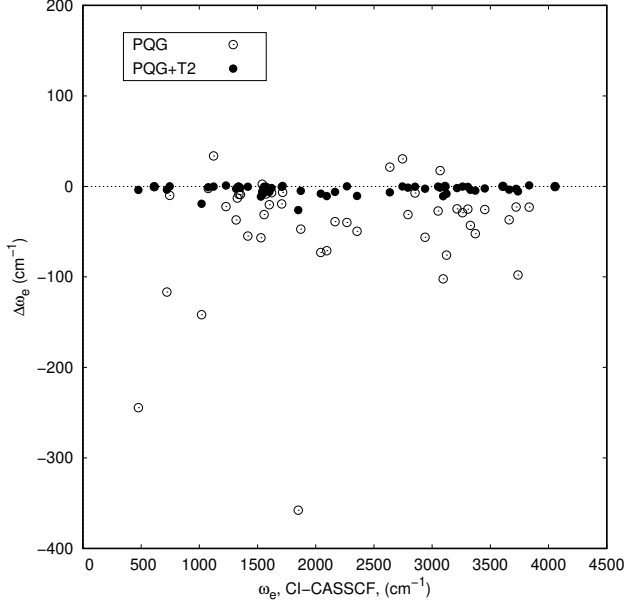
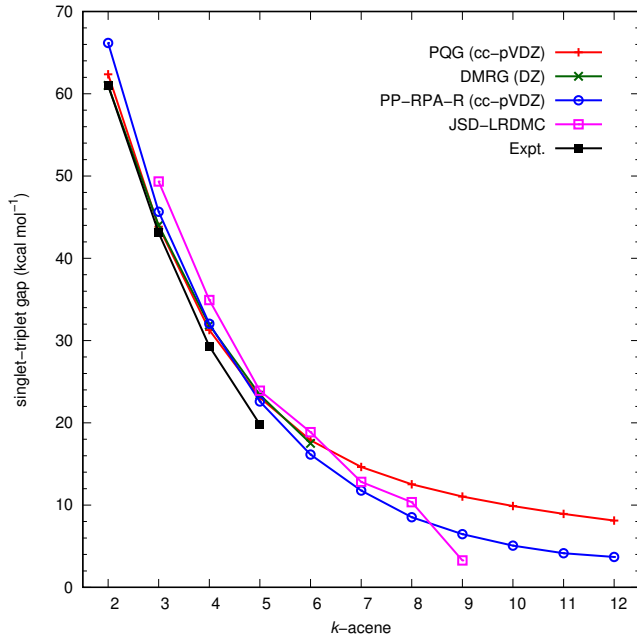


FIG. 3: Adiabatic singlet-triplet excitation energies for v2RDM-CASSCF PQG, DMRG-CASCI,[75] and JSD[82] along with vertical excitation energies using particle-particle random phase approximation[81] and experimental excitation energies.[83–86]

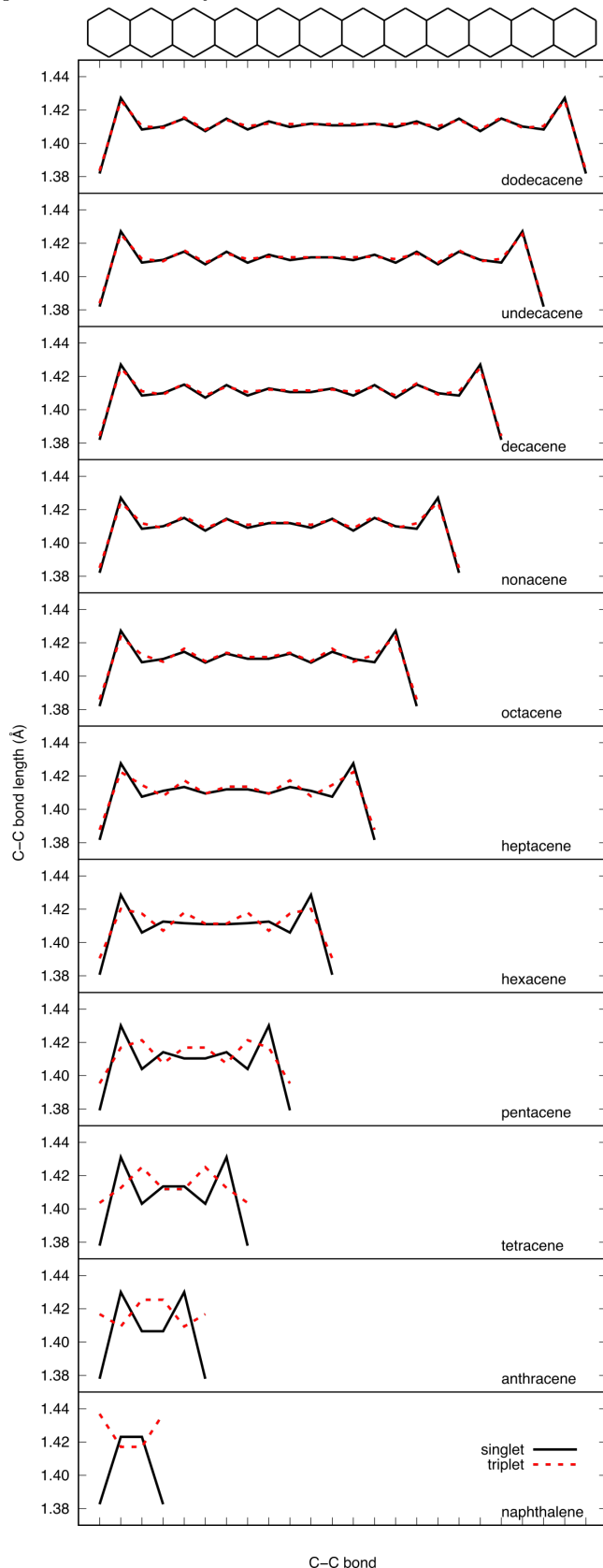


the series. Using the simple exponential decay formula  $E = ae^{-n/b} + c$ , the PQG estimate of the gap at the infinitely-long-molecule limit is 7.8 kcal mol<sup>-1</sup>. This value is slightly larger than that recently estimated[81] using PP-RPA, but direct comparisons to this and other values is complicated for several reasons. First, the PP-RPA excitation energies presented in Ref. 81 are vertical; the singlet and triplet energies reproduced in Fig. 3 were evaluated at the singlet geometry, which was optimized using restricted B3LYP (hence, the “R” in PP-RPA-R). Second, comparisons to JSD are difficult because the JSD curve is far from smooth, and the second kink at nonacene can be attributed to the fact that this particular geometry was optimized at the JSD level of theory, while all of the other geometries were optimized using DFT (with the B3LYP functional).[82] Nonetheless, it does appear that the lack of dynamical correlation effects in our computations may lead to an overestimation of the singlet-triplet energy gap in the limit of infinitely long acene molecules.

Figure 4 shows the bond length alternation (BLA) for the C–C bonds along the long edge of each member of the linear polyacene series. The equilibrium cartesian coordinates are provided in the Supporting Information. In general, the alternation appears greatest toward the outer parts of the molecules, with smaller changes in the middle of the molecules; this trend applies to both the singlet and triplet states and is in agreement with previous work. For dodecacene, the C–C bond lengths lie within the range of 1.38 Å to 1.43 Å and approach a bond length of 1.41 Å in the center of the molecule. This bond equalization, which has been reported previously,[87, 88] is more noticeable in the geometry for the triplet state. Dupuis *et al.*[82] note that the equalization is associated with the localization of charge along the edges of the acene molecule, which, for the singlet state, is a signature of an antiferromagnetic arrangement of electrons that could be described as a di- or even polyradical. The central C–C bond length limit of 1.41 Å predicted by PQG is consistent with the limit of 1.406 Å separately reported using a spin-polarized DFT[87] and a DMRG valence bond model.[88]

For the smaller members of the series, the BLA pattern is qualitatively different for the singlet and triplet states, but, as the length of the molecules increases, the singlet and triplet BLA patterns become more similar. These results contrast with the JSD-derived geometry for nonacene presented in Ref. 82. For JSD, the BLA pattern for the singlet and triplet states of nonacene clearly differ, and large oscillations (on the order of 0.02 Å for the triplet) persist in the center of the molecule. Since the JSD wave function describes dynamical correlation effects not captured by v2RDM-CASSCF, it is tempting to attribute these differences to a lack of dynamical correlation in the present computations. However, we observe similar agreement between the BLA patterns of the singlet and triplet states as described by unrestricted B3LYP, which *only* captures dynamical corre-

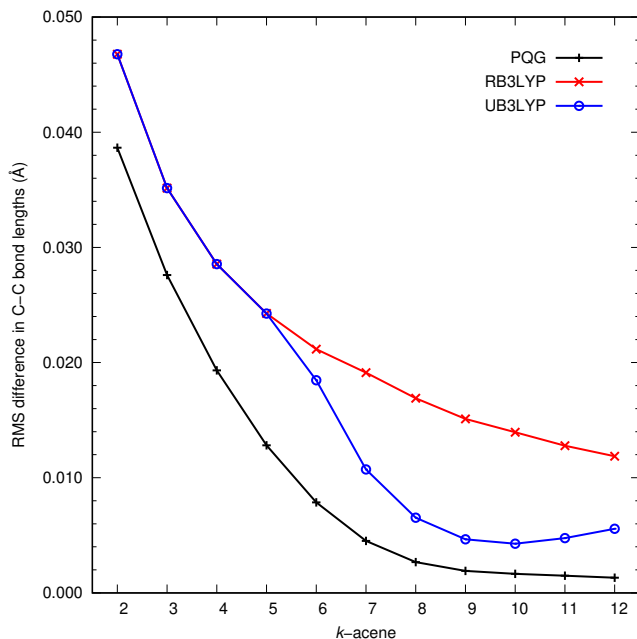
FIG. 4: C–C bond lengths ( $\text{\AA}$ ) along the long edge of the linear polyacene molecules. Results are presented for the lowest-energy singlet and triplet states computed at the PQG/cc-pVDZ level of theory.



lation effects. Rather, the discrepancies between JSD and PQG can be traced to a lack of static correlation effects in the former method. This hypothesis is partially confirmed by the Jastrow double determinant (JDD) description of the geometry of the singlet state of nonacene, also provided in Ref. 82. JDD captures some static correlation effects that are missing in JSD, and differences between the predictions of JSD and JDD can be used to quantify whether or not the longer members of the acene series have open-shell singlet character. For the singlet state, JDD predicts that alternations in bond lengths are most apparent at the edge of the molecule, in agreement with the present PQG results. However, Ref. 82 also provides results using the Jastrow antisymmetric geminal power (JAGP) wave function that are more in line with those of JSD. The JAGP *ansatz* captures captures static correlation effects beyond those described by JDD, and, apparently, these additional considerations lead to a reduction in the open-shell character of the singlet state, as well as a commensurate reduction in the charge localization along the edges of the acene molecules. These observations, which are outlined in Ref. 82, are consistent with those of Ref. 89, which employed a coupled-cluster valence-bond singles and doubles (CCVB-SD) description of the valence space. At the CCVB-SD level of theory, the polyradical nature of the longer members of the linear polyacene series is significantly reduced when the  $\sigma$ -network is correlated alongside the  $\pi$ -network, as compared to the case where the  $\pi$ -network alone is correlated. Because our active space consists of only the  $\pi$ -network, signatures of polyradical character, such as the equalization of the BLA reported here and the natural orbital occupation numbers reported elsewhere,[48, 51] may be exaggerated.

We can further quantify the similarities between the singlet and triplet structures by comparing the root mean square (RMS) difference in the C–C bond lengths along the long edge of each linear acene molecule. Figure 5 illustrates this quantity using structures obtained at the PQG/cc-pVDZ and B3LYP/cc-pVDZ (restricted and unrestricted) levels of theory. The RMS difference in the bond lengths decreases monotonically for both restricted B3LYP and PQG, with the PQG value falling to less than  $0.002 \text{ \AA}$  at dodecacene. On the other hand, from this metric, it appears that the singlet and triplet states of the longer members of the series are predicted to have quite different geometries at the restricted B3LYP level of theory. Indeed, when we look at the BLA patterns for restricted B3LYP, we find that this method recovers some of the characteristics of the nonacene geometry from JSD: (i) large changes in the bond lengths persist into the middle of the molecules, and (ii) the BLA patterns for the singlet and triplet states are qualitatively different. For molecules as large or larger than hexacene, spin-broken B3LYP solutions for the singlet states becomes energetically favorable, which leads to significant decreases in the RMS difference in the bond lengths.

FIG. 5: Root mean square (RMS) difference between the C–C bond lengths along the long edge of the linear polyacene molecules, as optimized for the lowest-energy singlet and triplet states.



## V. CONCLUSIONS

We have presented an implementation of analytic energy gradients for the v2RDM-driven CASSCF method using the density-fitting approximation to the electron repulsion integrals. Benchmark calculations for equilibrium geometries and harmonic vibrational frequencies indicate that v2RDM-CASSCF performs as well as CI-CASSCF in reproducing experimental results for a test set of small molecules. When the two-particle  $N$ -representability conditions are enforced, geometries and frequencies generally agree with those from CI-CASSCF, and significantly improved results are obtained when also enforcing three-particle  $N$ -representability conditions (T2). In the current implementation, enforcing the PQG and T2 conditions requires  $\mathcal{O}(n^6)$  and  $\mathcal{O}(n^9)$ , floating-point operations, respectively, where  $n$  is the number of active space orbitals. For large-scale applications, the PQG conditions may be the only practically

enforceable ones; fortunately, the present benchmark calculations indicate that these conditions should be adequate for equilibrium geometries. Some care should be taken, however, should one wish to compute harmonic frequencies under the PQG conditions alone.

The DF approximation facilitates the evaluation of v2RDM-CASSCF analytic energy gradients for large molecules with active spaces that are much larger than those that existing CI-CASSCF implementations can reasonably consider. We demonstrated this capability by optimizing the geometries for the lowest-energy singlet and triplet states of the linear polyacene series up to dodecacene. Using these optimized structures, we evaluated the adiabatic singlet-triplet energy gaps for the series and found that the v2RDM-CASSCF gap converges to 7.8 kcal mol<sup>-1</sup> in the limit of an infinitely-long acene molecule; this estimate is larger than estimates from other methods that include dynamical correlation effects, such as the particle-particle random phase approximation. We also demonstrated that v2RDM-CASSCF predicts increasingly similar structures for the lowest-energy singlet and triplet states as the length of the acene molecules increases. This similarity is a signature of the open-shell nature of the singlet state. We caution, however, that several recent analyses[82, 89] suggest that the limited consideration of nondynamical correlation effects can lead to qualitatively different results than more rigorous considerations. In the present context, a more rigorous description of the system might include an expanded active space that incorporates some portion of the  $\sigma$ -network. Even then, a complete description of the system should include dynamical correlation effects beyond those inadvertently captured by large-active-space v2RDM-CASSCF.

**Supporting information.** Harmonic vibrational frequencies computed at the PQG/cc-pVDZ level of theory using “loose” and “tight” convergence criteria, equilibrium structures for the linear polyacene series computed at the PQG/cc-pVDZ level of theory, and C–C bond lengths for the long edge of the linear polyacene molecules up to dodecacene.

**Acknowledgments.** This material is based upon work supported by the Army Research Office Small Business Technology Transfer (STTR) program under Grant No. 65925CHST1.

- 
- [1] B. O. Roos and P. R. Taylor, *Chem. Phys.* **48**, 157 (1980).
  - [2] P. Siegbahn, A. Heiberg, B. Roos, and B. Levy, *Phys. Scr.* **21**, 323 (1980).
  - [3] P. E. M. Siegbahn, J. Almlöf, A. Heiberg, and B. O. Roos, *J. Chem. Phys.* **74**, 2384 (1981).
  - [4] B. O. Roos, *Advances in Chemical Physics; Ab Initio Methods in Quantum Chemistry Part 2* (John Wiley and Sons, Ltd., 1987), vol. 69, pp. 399–445.
  - [5] K. Andersson, P. A. Malmqvist, B. O. Roos, A. J. Sadlej, and K. Wolinski, *J. Phys. Chem.* **94**, 5483 (1990).

- [6] K. D. Vogiatzis, D. Ma, J. Olsen, L. Gagliardi, and W. A. de Jong, *J. Chem. Phys.* **147**, 184111 (2017), URL <https://doi.org/10.1063/1.4989858>.
- [7] J. Olsen and B. O. Roos, *J. Chem. Phys.* **89**, 2185 (1988).
- [8] P. A. Malmqvist, A. Rendell, and B. O. Roos, *J. Phys. Chem.* **94**, 5477 (1990).
- [9] T. Fleig, J. Olsen, and C. M. Marian, *J. Chem. Phys.* **114**, 4775 (2001).
- [10] D. Ma, G. L. Manni, and L. Gagliardi, *J. Chem. Phys.* **135**, 044128 (2011).
- [11] G. L. Manni, D. Ma, F. Aquilante, J. Olsen, and L. Gagliardi, *J. Chem. Theory Comput.* **9**, 3375 (2013).
- [12] J. Ivanic, *J. Chem. Phys.* **119**, 9364 (2003).
- [13] R. E. Thomas, Q. Sun, and G. H. Booth, *J. Chem. Theory Comput.* **11**, 5316 (2015).
- [14] G. L. Manni, S. D. Smart, and A. Alavi, *J. Chem. Theory Comput.* **12**, 1245 (2016).
- [15] S. R. White, *Phys. Rev. Lett.* **69**, 2863 (1992).
- [16] S. R. White, *Phys. Rev. B* **48**, 10345 (1993).
- [17] U. Schollwöck, *Rev. Mod. Phys.* **77**, 259 (2005).
- [18] U. Schollwöck, *Ann. Phys.* **326**, 96 (2011).
- [19] A. O. Mitrushenkov, R. Linguerri, and P. Palmieri, *J. Chem. Phys.* **119**, 4148 (2003).
- [20] G. K.-L. Chan and M. Head-Gordon, *J. Chem. Phys.* **116**, 4462 (2002).
- [21] K. H. Marti, I. M. Ondik, G. Moritz, and M. Reiher, *J. Chem. Phys.* **128**, 014104 (2008).
- [22] D. Zgid and M. Nooijen, *J. Chem. Phys.* **128**, 014107 (2008).
- [23] Y. Kurashige and T. Yanai, *J. Chem. Phys.* **130**, 234114 (2009).
- [24] R. Olivares-Amaya, W. Hu, N. Nakatani, S. Sharma, J. Yang, and G. K.-L. Chan, *J. Chem. Phys.* **142**, 034102 (2015).
- [25] S. Szalay, M. Pfeiffer, V. Murg, G. Barcza, F. Verstraete, R. Schneider, and O. Legeza, *Int. J. Quantum Chem.* **115**, 1342 (2015).
- [26] S. Wouters and D. V. Neck, *Eur. Phys. J. D* **68**, 272 (2014).
- [27] S. Knecht, E. D. Hedegard, S. Keller, A. Kovyrshin, Y. Ma, A. Muolo, C. J. Stein, and M. Reiher, *Chimia* **70**, 244 (2016).
- [28] D. Ghosh, J. Hachmann, T. Yanai, and G. K.-L. Chan, *J. Chem. Phys.* **128**, 144117 (2008).
- [29] T. Yanai, Y. Kurashige, D. Ghosh, and G. K.-L. Chan, *Int. J. Quantum Chem.* **109**, 2178 (2009).
- [30] T. Yanai, Y. Kurashige, E. Neuscamman, and G. K.-L. Chan, *J. Chem. Phys.* **132**, 024105 (2010).
- [31] S. Wouters, W. Poelmans, P. W. Ayers, and D. V. Neck, *Comput. Phys. Commun.* **185**, 1501 (2014).
- [32] Q. Sun, J. Yang, and G. K.-L. Chan, *Chem. Phys. Lett.* **683**, 291 (2017).
- [33] Y. Ma, S. Knecht, S. Keller, and M. Reiher, *J. Chem. Theory Comput.* **13**, 2533 (2017).
- [34] C. Garrod and J. K. Percus, *J. Math. Phys.* **5**, 1756 (1964).
- [35] C. Garrod, M. V. Mihailović, and M. Rosina, *J. Math. Phys.* **16**, 868 (1975).
- [36] M. V. Mihailović and M. Rosina, *Nucl. Phys. A* **237**, 221 (1975).
- [37] M. Rosina and C. Garrod, *J. Comp. Phys.* **18**, 300 (1975).
- [38] R. M. Erdahl, C. Garrod, B. Golli, and M. Rosina, *J. Math. Phys.* **20**, 1366 (1979).
- [39] R. M. Erdahl, *Rep. Math. Phys.* **15**, 147 (1979).
- [40] M. Nakata, H. Nakatsuji, M. Ehara, M. Fukuda, K. Nakata, and K. Fujisawa, *J. Chem. Phys.* **114**, 8282 (2001).
- [41] D. A. Mazziotti and R. M. Erdahl, *Phys. Rev. B* **63**, 042113 (2001).
- [42] D. A. Mazziotti, *Phys. Rev. B* **65**, 062511 (2002).
- [43] D. A. Mazziotti, *Phys. Rev. B* **74**, 032501 (2006).
- [44] Z. Zhao, B. J. Braams, M. Fukuda, M. L. Overton, and J. K. Percus, *J. Chem. Phys.* **120**, 2095 (2004).
- [45] M. Fukuda, B. J. Braams, M. Nakata, M. L. Overton, J. K. Percus, M. Yamashita, and Z. Zhao, *Math. Program., Ser. B* **109**, 553 (2007).
- [46] E. Cancès, G. Stoltz, and M. Lewin, *J. Chem. Phys.* **125**, 064101 (2006).
- [47] B. Verstichel, H. V. Aggelen, D. V. Neck, P. W. Ayers, and P. Bultinck, *Phys. Rev. B* **80**, 032508 (2009).
- [48] J. Fosso-Tande, D. R. Nascimento, and A. E. DePrince, *Mol. Phys.* **114**, 423 (2016).
- [49] B. Verstichel, H. van Aggelen, D. V. Neck, P. Bultinck, and S. D. Baerdemacker, *Comput. Phys. Commun.* **182**, 1235 (2011).
- [50] G. Gidofalvi and D. A. Mazziotti, *J. Chem. Phys.* **129**, 134108 (2008).
- [51] J. Fosso-Tande, T.-S. Nguyen, G. Gidofalvi, and A. E. DePrince, *J. Chem. Theory Comput.* **12**, 2260 (2016).
- [52] E. Maradzike, G. Gidofalvi, J. M. Turney, H. F. Schaefer, and A. E. DePrince, *J. Chem. Theory Comput.* **13**, 4113 (2017).
- [53] [https://github.com/edeprince3/v2r2dm\\_casscf](https://github.com/edeprince3/v2r2dm_casscf).
- [54] J. M. Turney, A. C. Simmonett, R. M. Parrish, E. G. Hohenstein, F. A. Evangelista, J. T. Fermann, B. J. Mintz, L. A. Burns, J. J. Wilke, M. L. Abrams, et al., *WIREs Comput. Mol. Sci.* **2**, 556 (2012).
- [55] R. M. Parrish, L. A. Burns, D. G. A. Smith, A. C. Simmonett, A. E. DePrince, E. G. Hohenstein, U. Bozkaya, A. Y. Sokolov, R. D. Remigio, R. M. Richard, et al., *J. Chem. Theory Comput.* **13**, 3185 (2017).
- [56] J. L. Whitten, *J. Chem. Phys.* **58**, 4496 (1973).
- [57] B. I. Dunlap, J. W. D. Connolly, and J. R. Sabin, *J. Chem. Phys.* **71**, 3396 (1979).
- [58] M. Feyereisen, G. Fitzgerald, and A. Komornicki, *Chem. Phys. Lett.* **208**, 359 (1993).
- [59] O. Vahtras, J. Almlöf, and M. W. Feyereisen, *Chem. Phys. Lett.* **213**, 514 (1993).
- [60] Y. Shao, Z. Gan, E. Epifanovsky, A. T. Gilbert, M. Wormit, J. Kussmann, A. W. Lange, A. Behn, J. Deng, X. Feng, et al., *Mol. Phys.* **113**, 184 (2015), URL <https://doi.org/10.1080/00268976.2014.952696>.
- [61] A. J. Coleman, *Rev. Mod. Phys.* **35**, 668 (1963).
- [62] R. M. Erdahl, *Int. J. Quantum Chem.* **13**, 697 (1978).
- [63] H. van Aggelen, B. Verstichel, P. Bultinck, D. V. Neck, and P. W. Ayers, *J. Chem. Phys.* **136**, 014110 (2012).
- [64] J. Povh, F. Rendl, and A. Wiegele, *Computing* **78**, 277 (2006).
- [65] J. Malick, J. Povh, F. Rendl, and A. Wiegele, *SIAM J. Optim.* **20**, 336 (2009).
- [66] D. A. Mazziotti, *Phys. Rev. Lett.* **106**, 083001 (2011).
- [67] F. Weigend and M. Häser, *Theor. Chem. Acc.* **97**, 331 (1997).
- [68] J. E. Rice, R. D. Amos, N. C. Handy, T. J. Lee, and H. F. S. III, *J. Chem. Phys.* **85**, 963 (1986).
- [69] M. W. Schmidt, K. K. Baldrige, J. A. Boatz, S. T. Elbert, M. S. Gordon, J. H. Jensen, S. Koseki, N. Matsunaga, K. A. Nguyen, S. Su, et al., *J. Comput. Chem.*

- 14, 1347 (1993).
- [70] T. H. Dunning, J. Chem. Phys. **90**, 1007 (1989).
  - [71] F. Weigend, Phys. Chem. Chem. Phys. **4**, 4285 (2002).
  - [72] R. D. Johnson III, *Nist computational chemistry comparison and benchmark database*, release 16a, August 2013.
  - [73] K. N. Houk, P. S. Lee, and M. Nendel, J. Org. Chem. **66**, 5517 (2001).
  - [74] M. Bendikov, H. M. Duong, K. Starkey, K. N. Houk, E. A. Carter, and F. Wudl, J. Am. Chem. Soc. **126**, 7416 (2004).
  - [75] J. Hachmann, J. J. Dorando, M. Avilés, and G. K.-L. Chan, J. Chem. Phys. **127**, 134309 (2007).
  - [76] K. Pelzer, L. Greenman, G. Gidofalvi, and D. A. Mazziotti, J. Phys. Chem. A **115**, 5632 (2011).
  - [77] W. Mizukami, Y. Kurashige, and T. Yanai, J. Chem. Theory Comput. **9**, 401 (2013).
  - [78] F. Plasser, H. Pašalić, M. H. Gerzabek, F. Libisch, R. Reiter, J. Burgdörfer, T. Müller, R. Shepard, and H. Lischka, Angew. Chem. Int. Ed. **52**, 2581 (2013).
  - [79] S. Horn, F. Plasser, T. Müller, F. Libisch, J. Burgdörfer, and H. Lischka, Theor. Chem. Acc. **133**, 1511 (2014).
  - [80] S. Horn and H. Lischka, J. Chem. Phys. **142**, 054302 (2015).
  - [81] Y. Yang, E. R. Davidson, and W. Yang, Proc. Natl. Acad. Sci. U. S. A **113**, E5098 (2016).
  - [82] N. Dupuy and M. Casula, J. Chem. Phys. **148**, 134112 (2018).
  - [83] J. B. Birks, Photophysics of Aromatic Molecules Wiley, London, (1970).
  - [84] J. Burgos, M. Pope, C. E. Swenberg, and R. R. Alfano, Phys. Status Solidi B **83**, 249 (1977).
  - [85] N. Sabbatini, M. T. Indelli, M. T. Gandolfi, and V. Balzani, J. Phys. Chem. **86**, 3585 (1982).
  - [86] J. Schiedt and R. Weinkauff, Chem. Phys. Lett. **266**, 201 (1997).
  - [87] D. Jiang and S. Dai, J. Phys. Chem. A **112**, 332 (2008).
  - [88] Z. Qu, D. Zhang, C. Liu, and Y. Jiang, J. Phys. Chem. A **113**, 7909 (2009).
  - [89] J. Lee, D. W. Small, E. Epifanovsky, and M. Head-Gordon, J. Chem. Theory Comput. **13**, 602 (2017), URL <https://doi.org/10.1021/acs.jctc.6b01092>.